Mathematical Statistician and Engineering Applications
ISSN: 2094-0343
2326-9865

Dy Substituted $Bifeo_3$ Nanoparticals: Itsoptical, Structural, Dielectric, Magnetic Properties

Kotha Lakshmana Gupta1*, [2]Sonali Saha

[1]Research Scholar, Dept. of Physics
IES University Bhopal,Madhya Pradesh, India
[2]Research Guide, Dept. of Physics
IES University Bhopal,Madhya Pradesh, India

Article Info
Page Number: 12263-12282
Publication Issue:
Vol. 71 No. 4 (2022)

Article History
Article Received: 15 September 2022
Revised: 24 October 2022
Accepted: 18 November 2022
Publication: 21 December 2022

Abstract
Time-tested materials, such as ferroelectric or magnetic, have led to some of the most significant technical advancements of our day. Off-centre structural distortions and local spins are linked to ferroelectricity and magnetism, respectively. BFO nanoparticles with increased multiferroic characteristics are discussed in this research. Zr4+ doping of BFO nanoparticles has been shown to alter their structural characteristics, resulting in better magnetic and dielectric properties. Structural analysis results demonstrate that Zr4+ doping has a direct impact on the magnetic properties of produced nanoparticles, as well as on the dielectric and optical characteristics.
Keywords: Dielectric, Nanoparticles, Optical, Ferroelectric, Magnetic.

Since it has a lot of potential for use in cutting-edge devices and intriguing physics, the field of multiferroic materials has gained a lot of attention [W. Eerenstein (2006); R, Ramesh et al, 2007]. As a result of its high ferroelectric Curie (TC1103 K) as well as antiferromagnetic Neel (TN643 K) temperatures, of most of the ABO3 multiferroic materials, BiFeO3 (BFO) has the most promise for a specific system.Due to the lengthy 62 nm periodicity of the controlled spiral spin structure as well as the G-type antiferromagnetic character, bulk BFO's macroscopic magnetization cannot be seen, ruling out the possibility of multiferroic features. . Thin films and nanoparticles have recently been shown to exhibit modest ferromagnetism due to the size effect. Rare earth (Pr3, Gd3, Ho3 & Dy3) and transition metal (Ti4 & Mn4) ions can be replaced at the A-site [B. Yu et al (2008); V.A. Khomchenko; N.V. Minh et al 2009; S. Zhang et al 2009] ions have been found to have a positive effect on the redox potential of the system. [M. Kumar et al. (2006)] ions of transition metal (Ti4; Mn4 ;) ions, magnetic properties can be improved. Adding magnetically active Dy_3 ions at the A-site stabilized the perovskitearchitecture just as improved the BFO's ferroelectric and magnetic characteristics Raman spectroscopy and optical characteristics of Dy-doped BFO bulk ceramics are rarely discussed in the literature. There was an immediate response from our research team to synthesize multiferroic ceramics and investigate their structure, magnetic properties, and optical characteristics.

Research Methodology

Fruitful amalgamation of Bi1-xDyxFeO3 nanoparticles for x = 0.03; 0.05; and 0.10 was

accomplished by the sol-gel process. Weaken HNO3 must be added to de-ionized water in minuscule volumes to break up the stoichiometric amounts of Bi(NO3)3.5H2O, Fe(NO3)3.9H2O, similarly as Dy(NO3)2.xH2O, separately. The tartaric acid was then added to the metal nitrates in a 1:2 molar concentration as a skin-lightening factor. The powders were calcined for two hours at temperatures ranging from 550°F to 700°F to remove any remaining water after being vaporized as well as left to dry at 1000°C. In the XRD (Philips X′pert), CuK radiation was utilised to analyze the crystal structure of the materials.It was done utilizingRietveld refinement software to simulate the XRD data (FULLPROF). Renishaw Raman spectrometer (514.5 nm, Ar^+ laser) was used to capture the Raman spectra. When it came to examining the microscopic structure, researchers used the Philips CM 10 transmission electron microscope (TEM). With a step size of 5°C, the impedance analyzer (PSM 1735) was used to conduct dielectric measurements on silver coated pellets in the temperature limit 40-400 degree Celcius. SQUID magnetometers were utilized to distinguish room temperature charge hysteresis (M-H) to investigate the magnetic qualities of the material. Perkin Elmer Spectrum BX-II FTIR spectra at a goal of 1 cm-1 were utilized to decide the bond making inside the materials.

Data Analysis

Structural Studies

X-Ray Diffraction Studies

Experiments on $Bi_{1-x}Dy_xFeO_3$nanoparticles yielded the XRD patterns seen in Figure 1. BFO's rhombohedral structure has been indexed by the diffraction planes (012, 104, 110, 006, 202, (024, 116, 122, (018), 301, (208), (220), (131), (036), (128), (134) for specimens for x = 0.03 just as 0.05, corrspondingly. Because to the kinetics of production, short duration impurity amplitudes pertaining to Bi2Fe4O9 and Bi24Fe2O39 have also been discovered [Xu J.M et al (2009)].

Figure 1

(a) XRD Trends for $Bi_{1-x}Dy_xFeO_3$nanoparticles with x=0.03, 0.05 and 0.10, (b) represents enlarge view

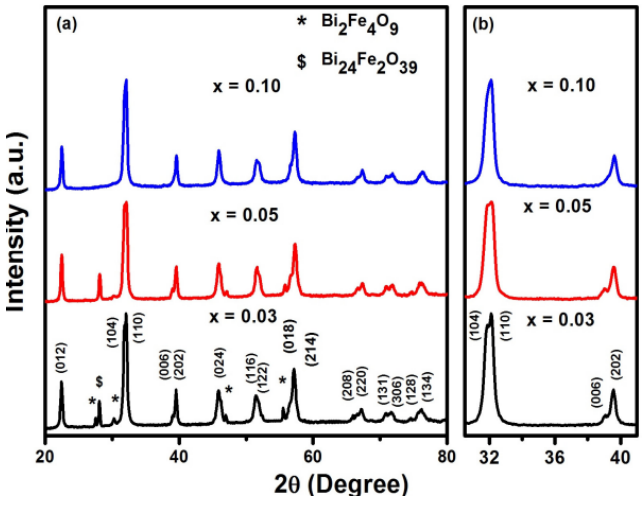

With increased Dy concentration, these impurity peaks disappeared. An R3c space group distortion is suggested by the presence of two different 2θ peak areas with 2 values about 32° and 39° for samples with and without x=0.03 and 0.05, respectively. The pinnacle parting conduct consistently lessens with expanding Dy focus. The two tops for (104) and (110); (006) and (202) planes are completely obvious on the XRD for x=0.03 and 0.05 examples, though the two tops for (104) and (110); (006) and (202) planes almost joined into a solitary expansive top for x=0.10 examples, proposing an organization driven change from rhombohedral to orthorhombic structure, as has been seen in other uncommon earth doped B tests. This plan stage progress from rhombohedral to orthorhombic is credited to the joining of Dy3+ particles in the design of BFO and the useful includes the development by the diminished molecule size.

Figure2

Rietveld refined XRD patterns for $Bi_{1-x}Dy_xFeO_3$ nanoparticles (a) x = 0.03 (b) 0.05 and (c) 0.10. (d) Every one of the specimens are plotted in a Williamson–Hall layout.

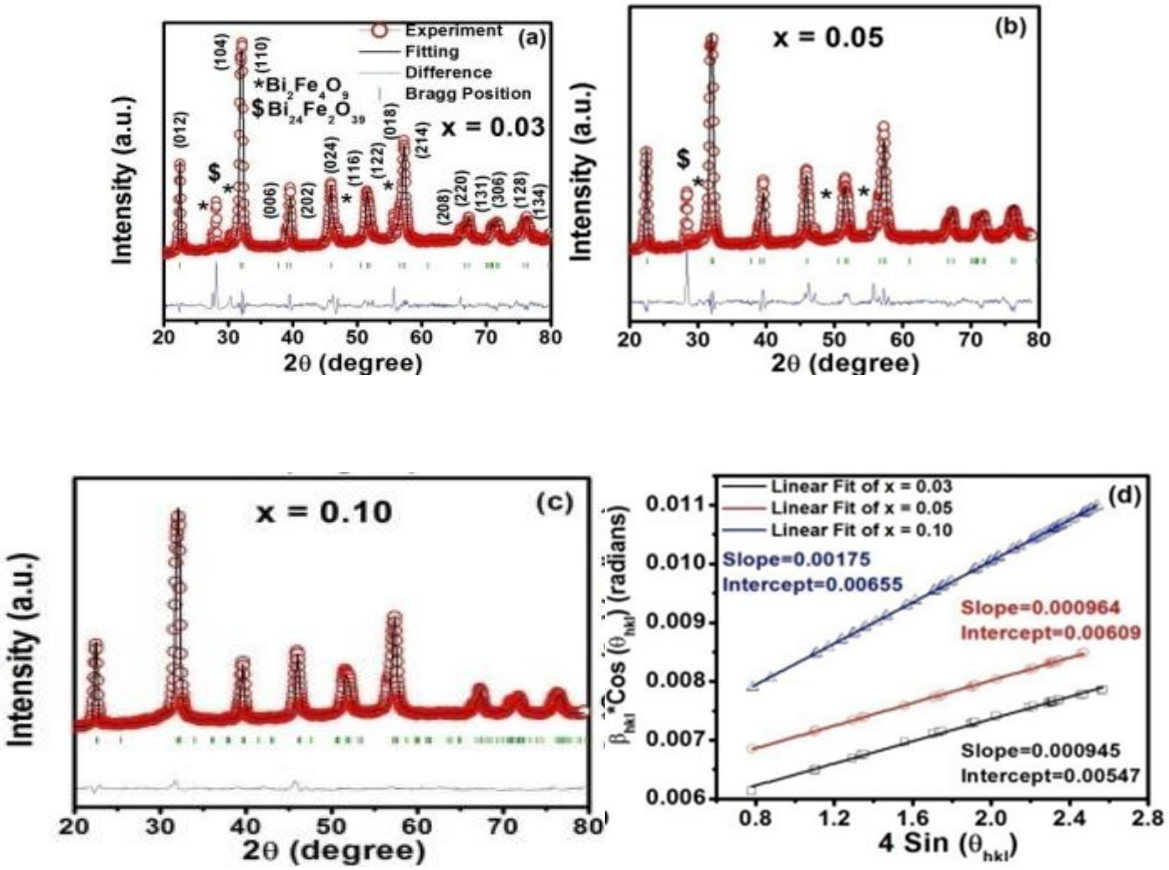

Figure 2 shows the refined specimen's Rietveld crystal architectures, which have been examined from FULLPROF software (a-c). By using Thompson–Cox–Hastings pseudo-Voigt capacity as well as linear interpolation between chosen background points, we were able to mimic Bragg peaks. We selected Pbnm space group with ionic positions for Bi/Dy and Fe at 4c, 4a, 4c as well as 8d in the Rietveld refinement for x=0.10 samples since the R3c space group had a better ionic position for those atoms, whereas the ionic position of oxygen in the R3c space group had a better one. The initial simulation was run with a few predetermined

parameters in mind. Finally, it was discovered that the measured and computed profiles agreed with each other after the last refining cycle. Rhombohedral structure is maintained for x=0.03, 0.05 as well as 0.10 specimens, but orthorhombic architecture is observed in the samples with x=0.10, according to fitting parameters. Table 1 lists the lattice parameters, atomic locations, bond lengths, and R factors derived through Rietveld refinement.

Table 1

Rietveld Structure characteristics for Bi1-xDyxFeO3 samples have been improved.

Compositions	**Variables of the matrix**	**Atoms**	**Positions**	**X**	**Y**	**z**	**Bond**	**Length (Å)**	**R-Factors (%)**
x = 0.03	a = 6.123 (Å) c = 14.802(Å) V = 369.99 (Å3)	Bi/Dy Fe O	6a 18b	0.0 0.0 0.4230	0.0 0.0 0.0484	0.0 0.2151 0.9598	Bi-O Fe-O	2.402 2.153	Rp = 4.42 Rwp = 6.09
x = 0.05	a = 4.565 (Å) c = 13.772 (Å) V = 369.35 (Å3)	Bi/Dy Fe O	6a 6a 18b	0.0 0.0 0.4216	0.0 0.0 -0.0054	0.0 0.2228 0.9540	Bi-O Fe-O	3.111 2.070	Rp= 6.21 Rwp = 8.76
x = 0.10	a = 5.543 (Å) b = 5.595 (Å) c = 7.843 (Å) V = 243.28 (Å3)	Bi/Dy Fe O1 O2	4c 4a 4c 8d	0.9784 0.5000 05000 0.7580	0.0044 0.0 0.5270 0.3649	0.2500 0.0 0.2500 0.0231	Bi-O Fe-O	2.4874 1.7656	Rp = 5.78 Rwp = 8.25

For $Bi_{1-x}Dy_xFeO_3$ nanoparticles, we used the Williamson–Hall method to compute the crystallite size as well as lattice point that is provided with the following expression:

$$\beta_{hkl}\cos\theta = \left[\frac{k\lambda}{D}\right] + 4\varepsilon\sin\theta \quad (1)$$

Where k is the structure factor, λ is X-beam frequency, Bragg's point, crystallite size D, strain ε, and βhkl is the absolute length at half most extreme. Figure 2 (d) shows how to plot the miniature strain and crystallite size utilizing a chart with 4 sin on the x-pivot and βklcos θ on the y-hub (D). For x=0.03, 0.05, and 0.10 examples, the anticipated crystallite sizes are 28.1, 25.2, and 23.5 nm, correspondingly.

To measure the degree to which A-site ions and B-site ions match, Goldschmidt developed the tolerance factor (t). The formula for calculating t's value is as follows:

$$t = \left((1-x)r_{Bi^{3+}} + xr_{Dy^{3+}} + r_{O^{2-}}\right) / \left(\sqrt{2}\left(r_{Fe^{3+}} + r_{O^{2-}}\right)\right) \quad (2)$$

Where$r_{Bi^{3+}}$, $r_{Dy^{3+}}$, $r_{Fe^{3+}}$ and $r_{O^{2-}}$ are the ionic half of the diameter of Bi^{3+}, Dy^{3+}, Fe^{3+} and O^{2-} ions correspondingly.

In an ideal perovskite crystal with a tolerance factor of one, the oxygen octahedron tilting inclination is 0. The values of "t" for x=0.03, 0.05, as well as 0.10 specimens are 0.888, 0.886, and 0.881, correspondingly. The deviation of "t" from 1 rises as the perovskite structure becomes more distorted. Substituting Dy^{3+} for Bi3+ would reduce the tolerance variableas well asrise the tilt angle of the octahedron, as Dy^{3+} has a lower ionic radius than Bi^{3+}. It is because of this compression and stretching of the Bi/Dy-O bond that the rhombohedral structure is transformed into an orthorhombic one when the distortion reaches a certain point. Figure 3 shows how the Dy concentration (x) affects the BFO lattice's lattice properties. It was discovered that when x increased, the lattice parameters decreased. The drop in lattice parameters is related to Bi^3greater +'s ionic radius (1.17) compared to Dy^3smaller +'s ionic radius (0.91).

Figure 3

Difference of matrix variable for $Bi_{1-x}Dy_xFeO_3$nanoparticles as a capacity of Dy concentration

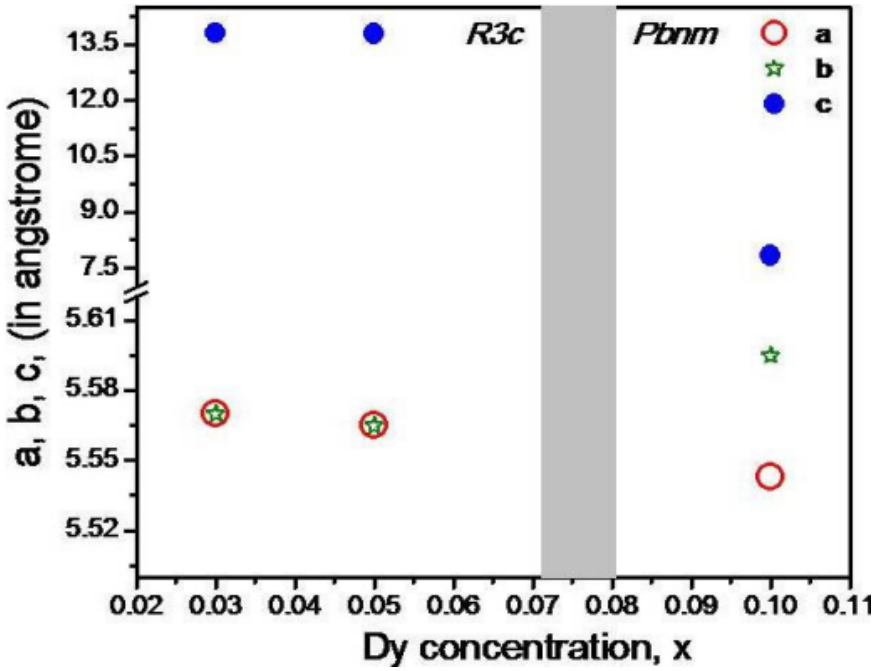

Raman Spectroscopy Studies

The probable structural alterations in $Bi_{1-x}Dy_xFeO_3$samples were investigated using Raman spectroscopy. For the Rhombohedral R3c layout, theory of group($\Gamma_{Raman} = 4A_1+9E$) forsee 13

Raman active modes [Singh M.K. et al. (2005)]. Samples with x=0.03 and 0.05 had all 13 ($4A_1$+9E) active modes, which is consistent with the group theory predictions for the R3c rhombohedral structure. Figure 4 shows Raman spectra for $Bi_{1-x}Dy_xFeO_3$ specimens with 10 active states in the band of 100-700 cm-1. The Raman mode assignment in this study agrees with Yang et al. [Yang Y. and colleagues (2008)]. There were four distinct peaks in the spectrum of the x=0.03 sample, all of which were ascribed to the A1-1, A1-2, A1-3, just as A1-4 modes, with the weakest peak located at 443 cm-1. When Dy ions are inserted into the BiFeO3 matrix, the symmetry of the lattice relaxes, the peaks widen and shift. Lone pair 6s2 electrons, which play a major role in the low frequency region, control ferroelectric ordering in BFO.

Figure 4 Room temperature Raman spectra of $Bi_{1-x}Dy_xFeO_3$nanoparticles.

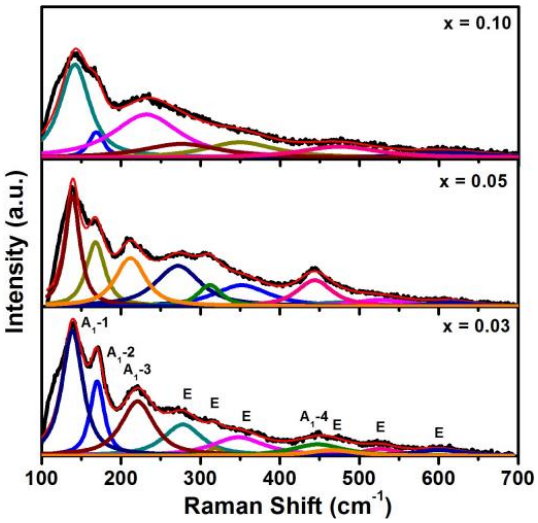

Total of the A1-1 through E-2 modes correspond to the covalent connection between Bi and O, whereas the higher frequency modes of E (>400 cm-1) are connected with Fe and O. The ionic masses and the force constant influence the Raman mode frequency. Because Dy^{3+} (162.5) has a lower mass than Bi3+ (208.98), the average mass at the A-site decreases when Dy ions are substituted, and as a result, the higher-frequency A1-1, A1-2, as well as A1-3 stages goes to the right. The shifts are caused by excessive lattice distortion caused by the competition among rhombohedral and orthorhombic architectures, widening, and merging of Raman modes. A comparison of the published and observed Raman results for $Bi_{1-x}Dy_xFeO_3$ nanoparticles is presented in Table 2

Table 2 This has been noticed and documented. Raman modes of Bi1-xDyxFeO3 ceramic with wavenumber 100-700 cm-1 at ambient temperature

Raman modes (cm-1)	**Yang et al. (cm-1)**	**x = 0.03 (cm-1)**	**x = 0.05 (cm-1)**	**x = 0.10 (cm-1)**
A1-1	141	140	139	142
A1-2	173	170	169	172

A1-3	217	217	218	229
A1-4	430	443	444	--
E	260	--	--	--
E	274	271	272	276
E	306	311	312	--
E	344	348	350	352
E	368	--	--	--
E	468	472	475	475
E	520	524	527	527
E	611	600	605	607

As part of the investigation of the BFO lattice's influence on Dy substitution, second-phonon Raman spectra have also been collected. Figure 5 (b-d) shows room temperature Raman spectra (a) as deconvoluted 2 phonon Raman spectra (b-d) for E-7, E-8, as well as E-9 typical Raman states (a). In the ordinary BFO Raman spectra, two phonon Raman stages show up at twofold movement levels of E7, E8, and E9 [Ramirez M.O. et al (2008)]. Due to the significant spin lattice coupling between nearby magnetic sublattices, two phonon modes have been seen in these samples. The 2 phonon stages shows the typical Gaussian groups at 977, 1100, as well as 1258 cm-1 with x=0.03 example, 982, 1102, as well as 1259 cm-1 for x=0.05 test, and 984, 1104, and 1260 cm-1 for x=0.10 example. Lesser recurrence E states (400 cm-1) and A1 modes have been connected to Bi-O1 holding, as per research [Pandit P et al (2011)].

Figure 5 (a) Raman spectra of $Bi_{1-x}Dy_xFeO_3$ nanoparticles at room temperature in the wavelength region 100-1400 cm-1 as well as (b)- (d) For x=0.03, 0.05, as well as 0.10 specimens, matched 2 phonon Raman patterns in the region 900-1400 cm-1 are shown.

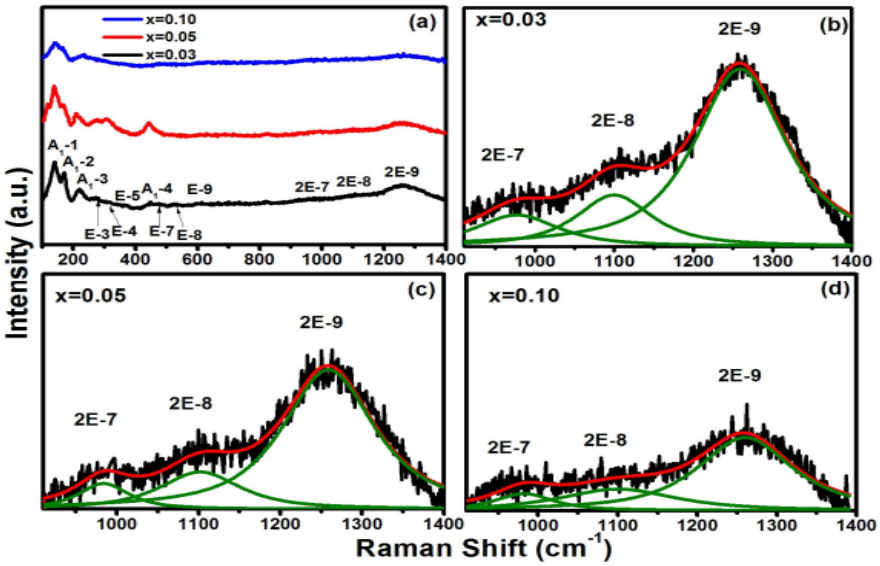

The more prominent reach E stages are conjectured to be brought about by Fe-O1 and Fe-O2 bonds, with O1 as well as O2 being pivotal yet additionally tropical particles, separately. Ramirez et al. credited suggestions 2E-8 and 2E-9 to Fe-O1 and Fe-O2 holding, separately, and related them to the octahedral revolution expected for weak ferromagnetism. Through the superexchange interaction, bond angles impact the antiferromagnetism in BFO. Spin-phonon interaction may be responsible for the distinct evolutions of two phonon overtones when the Raman spectra reflect the AFM structure's structural distortion. Overtone 2E-9's intensity decreases when Dy^{3+} concentration increases, as seen in Figure 5 (b-d). Because of underlying bending, the 2E-9 hint's solidarity has been diminished, which proposes turn two phonon coupling in the examples. Expanded Dy3+ focus might work on the magnetic qualities of x=0.03-0.10 examples, as per this twist two phonon coupling.

Morphological Studies

Figure 6

Transmission electron micrographs for $Bi_{1-x}Dy_xFeO_3$nanoparticles with (a) x=0.03, (b) x=0.05 as well as (c) x= 0.10 specimens. (d) Electron diffraction trend for an x=0.03 specimen in a chosen site.

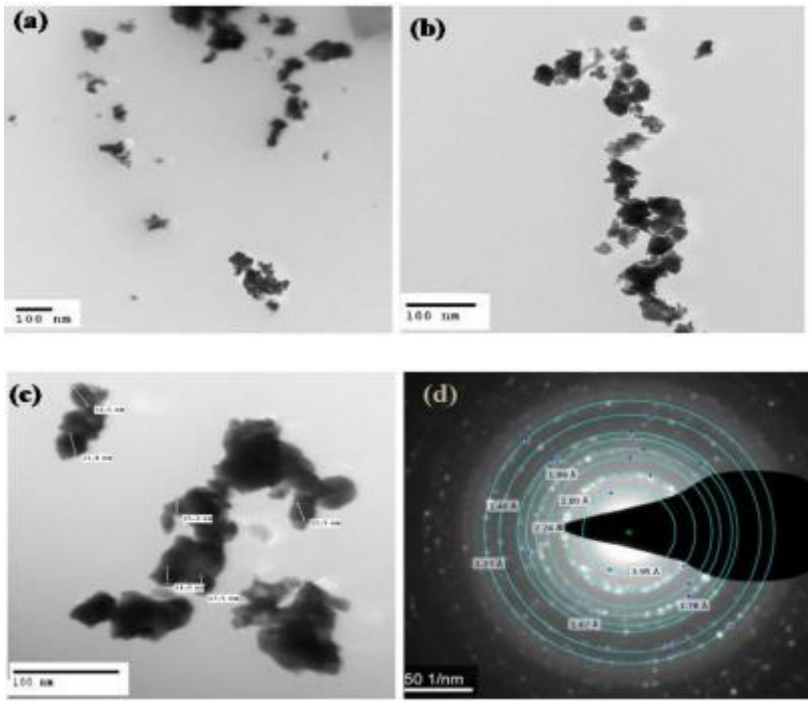

Studying particle morphology and the effect of Dy substitution on particle size was carried out using transmission electron microscopy (TEM). As the concentration of Dy3+ within BFO matrix increases, the average particle size of $Bi_{1-x}Dy_xFeO_3$samples decreases (Fig. 6 (a-c)). The plus of Dy^{3+} ions to the BFO matrixmay be responsible for the decrease in particle size [Watcharapasorn A. et al (2008)]. The particle size varies from 30 to 50 nm for x =0.03 & 0.05 specimens, but from 20 to 40 nm for x=0.10 specimens.Figure 6 shows the SAED trend for the x=0.03 specimen, which is displayed in the figure (d). The SAED picture reveals a beautiful dot pattern that clearly demonstrates the nanoparticles' extremely crystalline

structure. Lattice spacing is determined by analyzing the observed SAED pattern. In the xrd pattern of BFO, lattice spacings of 3.95, 2.80, 2.26, and 1.99 correspond to the (012), (110), (202), and (024) lattice planes.

MAGNETIC STUDIES

VSM and Squid Studies

The spiral spin structure of 62 nm of bulk BFO is well-known to have no effect on macroscopic magnetism. To free the latent magnetism trapped in the spiral installing the system, one method is to synthesize pure and doped BFO nanoparticles. To improve the magnetic characteristics of BFO nanoparticles, we synthesised Dy doped nanoparticles in this work. In addition, samples of BFO were sintered at 550 degree Celsius (for nanoparticles) as well as 700degree Celsius(for larger particles) to examine the influence of particle size on the magnetic characteristics of BFO (bulk). VSM and SQUID magnetometers were used to investigate the magnetic characteristics of Dy-doped BFO samples sintering at two different temperatures. Specimens sintered at 550degree Celsius, displayed in Fig.7 (a), demonstrate magnetization-magnetic field hysteresis loops (M-H). As illustrated in Figure 7, all samples sintering at 550°C exhibit typical ferromagnetic (superparamagnetic) ordering (a). Here, in Figure 7, you can see the M-H loops extended (b). An imperfect spin compensation between the two sublattices has been linked to the ferromagnetic (superparamagnetic) like behaviour with a high magnetization in antiferromagnetic nanoparticles. When antiferromagnetic nanoparticles are used, at the surface of the particle, lengthy antiferromagnetic equilibrium is frequently broken, resulting in increased magnetism due to insufficient spin compensation between two sublattices. From 0.03 to 0.10, the magnetic properties of BFO nanoparticles are further increased, demonstrating that the replacement of Dy^{3+} ions for Bismuth ferrite nanoparticles has an influence on magnetization. It has been determined that the MS for x = 0.03, 0.05, As well as 0.10 specimens ranges from 2.89 to 3.33 milliemu/g.

Figure 7

(a) Magnetization-magnetic field hysteresis (M-H) cycles for $Bi_{1-x}Dy_xFeO_3$specimens annealed at 550 degree Celsius at room temperature as well as (b) The increased view of the M-H loops.

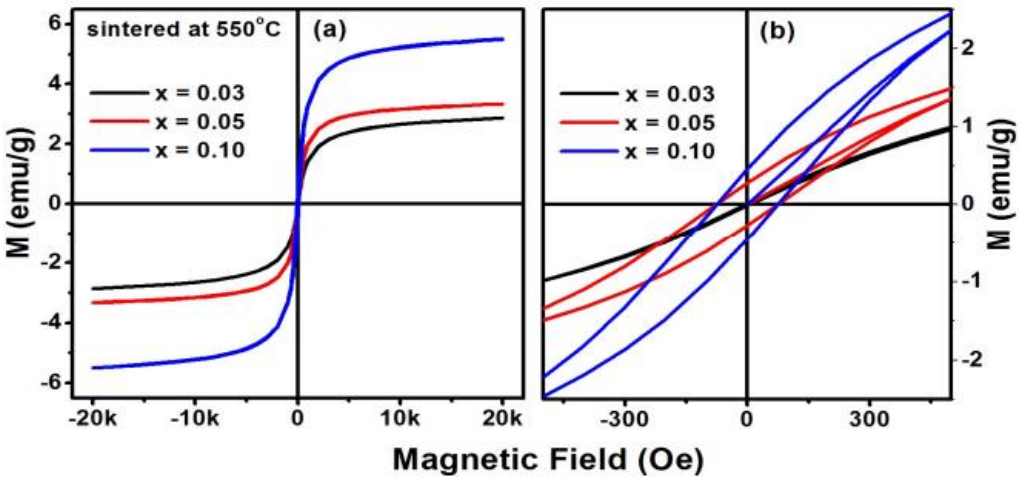

Figure 3 illustrates hysteresis loops for Dy doped samples annealed at 700 degree Celsius. Samples' magnetic characteristics were visibly affected by raising the sintering temperature (i.e., particle size). Raising the temperature from 550°C to 700°C has no effect on the loops' ability to withstand an applied magnetic field of 6 Tesla, while increasing the concentration of Dy from x=0.03 to 0.10 results in higher in magnetization. All of the samples had non-zero residual magnetization (M_r) and a coercive field (H_c). For x=0.03, 0.05, and 0.10 samples, the MH and M_r values are 0.57 as well as 0.0117 emu/g, 0.78 as well as 0.0177 emu/g, and 1.32 and 0.1315 emu/g, correspondingly.

Figure 8

Room temperature magnetization-magnetic field cycles for $Bi_{1-x}Dy_xFeO_3$ samples sintered in 700°C have been studied.

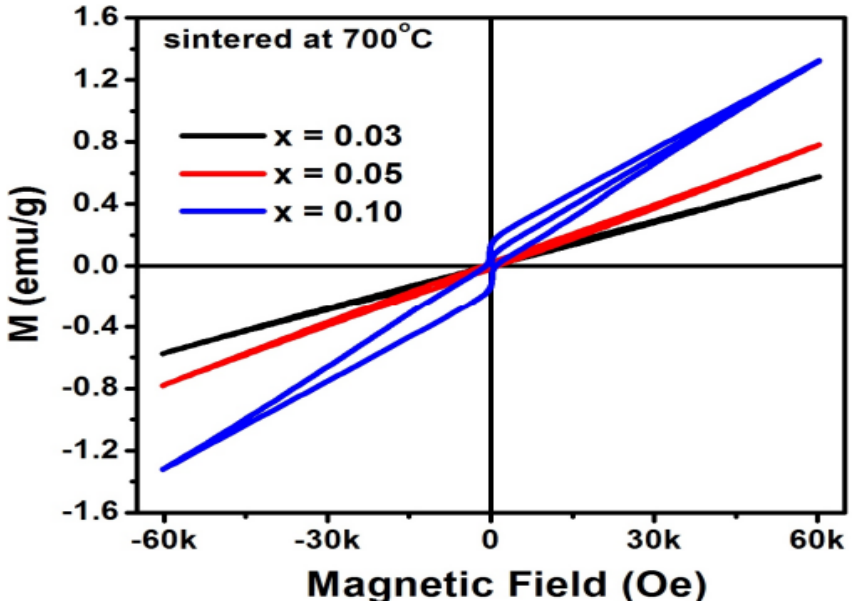

The coercive field (H_c) for x = 0.03, 0.05, as well as 0.10 samples is 679.930, 1166.855, as well as 987.664 O_e, respectively.Table 3 shows the magnetic properties of samples sintering at temperatures between 550°C and 700°C. Ho doped BFO (Jeon N. et al., 2011) has a similar double hysteresis loop for x=0.10, which shows that other causes are at play. Numerous mechanisms work together to increase net magnetization when Dy^{3+} ions are substituted. BFO's spin cycloid was disrupted and its structure was transformed from rhombohedral to orthorhombic when Dy^{3+} ions were substituted for bigger Bi^{3+} ones. This resulted in the release of latent magnetism.

The increase in magnetization was expected by the spin-two phonon coupling, as shown in the Raman spectra (Figure 5 (b-d)). So this increase in magnetization caused by structural deformation is compatible with Raman tests that demonstrate the coupling of spin-two phonons in the samples. It's also worth noting that Dy^{3+} has an extremely strong magnetism (μ_{eff} = 10.6μB) and when Dy^{3+} is substituted, Bi-O-Dy chains are created and these cohesions become magnetic sublattices [Qian FZ, et al. (2010)]. The unpaired electrons of the Dy^{3+} ion also contribute to the increased magnetization of the sample [Zhu W.M. et al. (2009)

Table 3

Magnetic parameters for $Bi_{1-x}Dy_xFeO_3$ samples

Constituents	Hc (Oe) 550°C	Mr (Oe) 550°C	MS (emu/g) 550°C	Hc (emu/g) 700°C	Mr (Oe) 700°C	MH (emu/g) 700°C
x = 0.03	5.20	0.01	2.95	680	0.012	0.57
x = 0.05	62.47	0.27	3.32	1166.85	0.018	0.80
x = 0.10	56.06	0.45	5.49	987.70	0.131	1.32

ELECTRIC STUDIES

Dielectric Studies

Dielectric loss (tan δ) and dielectric constant (ε') are illustrated in Figure 4.9 for $Bi_{1-x}Dy_xFeO_3$ nanoparticles at ambient temperature. From 100 Hz to 1 MHz, it has been shown that all samples show a decline in both the tan and the tan. Dc conductivity in the samples is shown by the low frequency dispersion in tan' andε'(Jonscher AK et al (1977)). There was a drop in the values ofε'and tanδfrom rising frequency in the lesser frequency band, whereas the esteems ofε'and tan δ remained practically constant at higher frequencies (>100 kHz). The Maxwell-Wagner model of interfacial space charge relaxation helps explain this variance in ε'. To put it another way: The dielectric constant is a result of oxygen (VO^{2+}) and bismuth (V_{Bi}^{3-}) vacancies that respond an applied electric field and contribute to the space charge. Relaxation is not possible at higher frequencies because they cannot keep up with the rapidly changing applied field. [Srivastava A et al. (2013)]. Low-frequency values of these parameters are bigger for samples with an x=0.03 value and drop accordingly for samples with an x=0.05 or 0.10 value.

Figure 9 Change of ε' as well as tan δ with frequency for $Bi_{1-x}Dy_xFeO_3$ nanoparticles at room temperature.

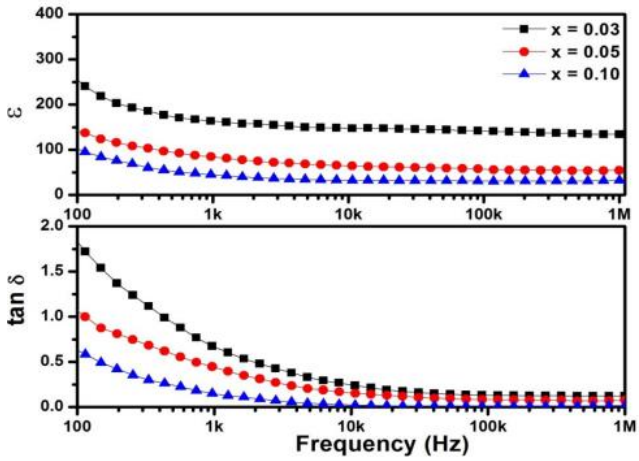

There is evidence that Dy^{3+} substitution helps to reduce leakage current by decreasing tan δ. Because of Bi3+ ions' volatile nature, the x=0.03 sample has a large ε' value because of the formation of oxygen - containing functional groups. Increased Dy^{3+} ion concentrations have reduced the volatilization of Bi^{3+} ions, which has resulted in lower ε' values [Makhdoom A.R et al (2012)] . In all samples, dielectric loss is very low at 100 Hz, in keeping with earlier studies [Kumar A et al (2012); Uniyal P et al (2009); Singh H et al (2012)], and the values of dielectric constant at that frequency are 236, 139, and 87, respectively]. For frequencies of 50 kHz, 100 kHz, and 1 MHz, Figures 10 and 1 exhibit the burden of temperatureof the dielectric constant (ε') as well as the dielectric loss (tanδ) for $Bi_{1-x}Dy_xFeO_3$samples. A discrepancy in dielectric constant was found at temperatures about 160°C for samples with x = 0.03 and 0.05. A brief connection among oxygen openings as well as the Fe^{3+}/Fe^{2+} redox pair may be responsible for this anomaly [Mishra R.K. et al (2008)]. [Catalan G. et al (2009)] claim that this anomaly is caused only by charge deficiencies and is not inherent to the type.

Figure 10

Variations in the dielectric constant (ε') with frequency for $Bi_{1-x}Dy_xFeO_3$nanoparticles with temperature dependency

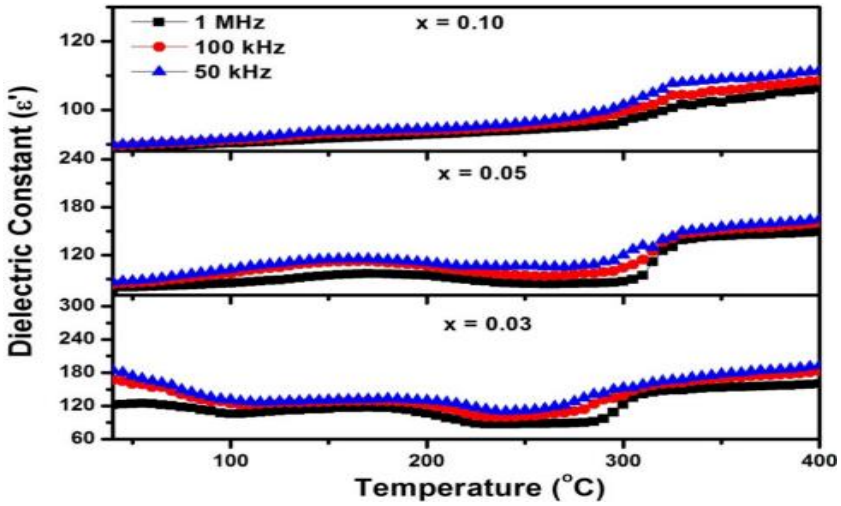

S_r and T_i codoped BFO has also been shown to exhibit comparable behaviour [Reetu et al (2011)]. At 160°C, the anomaly in the x=0.10 sample vanishes, showing that charge defects/oxygen holes are suppressed. It is advantageous to substitute part of the unpredictable Bi3+ particles with Dy3+ particles in BFO to consistent the unpredictability of the Fe3+/Fe2+ particle valence.

Around the Neel temperature, both the dielectric consistent ('ε') and dielectric misfortune have been viewed as extraordinarily high (TN). This sort of dielectric abnormality is brought about by vanishing magnetic request on electric request, as anticipated by the Landau-Devonshire speculation of stage change. This oddity in ε' and tan δ close to the antiferromagnetic Neel temperature demonstrates the presence of magnetoelectric coupling (ME).

Figure 11 Temperature-dependent changes in the dielectric loss (tanδ) of $Bi_{1-x}Dy_xFeO_3$ nanoparticles at various frequencies

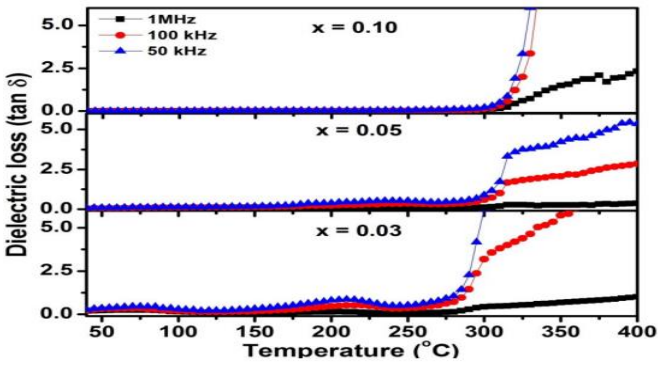

Conductivity Studies

The temperature-dependent ac conductivity of the materials was measured in order to better understand their conductivity. Fig. 12 shows the temperature-dependent ac conductivity at 10 kHz. An empirical relation can be used to determine the conductivity of a substance.

$$\sigma_{ac} = \varepsilon_o \varepsilon_r \omega \tan\delta \quad (3)$$

Tanδ is dielectric loss, εo is the vacuum permittivity, constant of dielectric is r, as well as ω is the angular frequency of the angular wave. In BFO, the concentration of Dy^{3+} decreased with decreasing temperature and increased ac. The increased mobility of oxygen vacancies may be to blame for the rise in conductivity as a function of rising temperature. As mobile charges, oxygen vacancies play a key role in oxide conductivity. The decrease in ac conductivity due to a decrease in oxygen vacancies is due to an increase in Dy^{3+} concentration. Based on a thermally activated process, activation energy (Ea) may be determined using the following equation.

$$\sigma_{ac} = \sigma_o \exp(-E_a/k_B T) \quad (4)$$

Figure 12 At 10 kHz, a.c. conductivity varies with the reverse of temperature for $Bi_{1-x}Dy_xFeO_3$ samples.

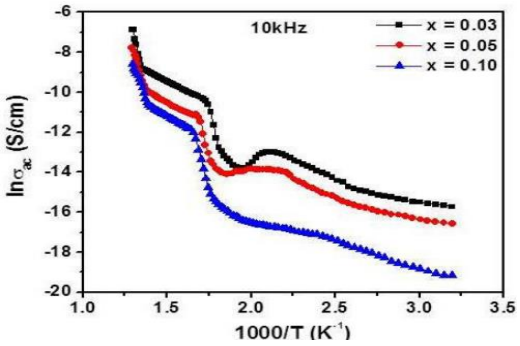

There is a pre-exponential factor kB and kB is the Boltzmann constant in this equation. For samples with x = 0.03, 0.05, and 0.10, the computed Ea values are 0.36, 0.39, and 0.44 eV. The values of Ea for x=0.03, 0.05, and 0.10 samples, on the other hand, are 0.13, 0.14, and

0.21 eV at low temperatures (40-110ºC). When Fe^{3+} and Fe^{2+} ions undergo multivalent oxidation (Fe3+/Fe^{2+} ions) when bismuth and oxygen vacancies coexist, ac conductivity increases. It is obvious that low-band mobility of O_2 openings contributes to the conduction procedure when the activation energy is larger at higher temperatures [Pandit P. et al (2011)].

OPTICAL STUDIES

UV-VIS Diffuse Absorption Studies

BFO's structural, electric, and magnetic characteristics have been the subject of various studies in the last few years. Studies on BFO's optical characteristics, on the other hand, are rare. The photocatalytic activity of organic molecules might also benefit from the use of BFO nanoparticles. The diffuse reflectance spectra (DRS) of all the $Bi_{1-x}Dy_xFeO_3$ nanoparticles were measured in the UV-visible range in order to learn more about their specific optical features. $Bi_{1-x}Dy_xFeO_3$nanoparticle diffuse reflectance spectra are given in Figure 13 in the UV-visible range. Every one of the formulations have the ability to absorb visible light in the 450-600 nm region. The optical band gap of the components was calculated using the tangent line in the figure of $(\alpha h\nu)_2$vshv [Chang D.A. et al(1995)]

$$\alpha h\nu = A(h\nu - E_g)^n \qquad (5)$$

Although Bismuth ferriteis a direct band gap item, we set n = 1/2. The x-axis extrapolation of the linear section of the curve yielded the band gap values for the samples. x=0.03, 0.05, and 0.10 resulted in band gaps of 2.12, 2.20, and 2.22 eV for the nanoparticles, which agrees well with the previously published values for BFO nanoparticles [Liu Z et al. (2010); Guo R. et al. (2010)]. . The octahedral distortion and molecular orbital rearrangement in $Bi_{1-x}Dy_xFeO_3$nanoparticles may be responsible for the narrowing of the band gap. The 370 nm bump is believed to be caused by charge transport from ligand to metal and metal to metal [Mukherjee A. et al. (2012)]. Crystal field transitions are linked to the 750 nm absorption band [Joshi U.A. et al. (2008)].

Nanoparticles that have been doped with Dy have a noticeable blue shift in their absorption spectra. The rise in band gap may be attributed to the mixing of dopants atoms, which affect the electrical architecture of nanoparticles, since the nanoparticles are larger than 10 nm, and therefore the observed blue shift.

Figure 13 (a) Ultra Voilet-Visible absorption spectra as well as (b) – (d) Tauc'sgraphs for Bi1-xDyxFeO3 nanoparticles

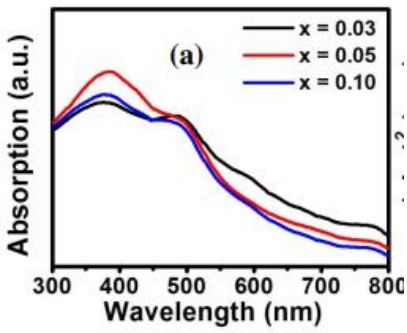

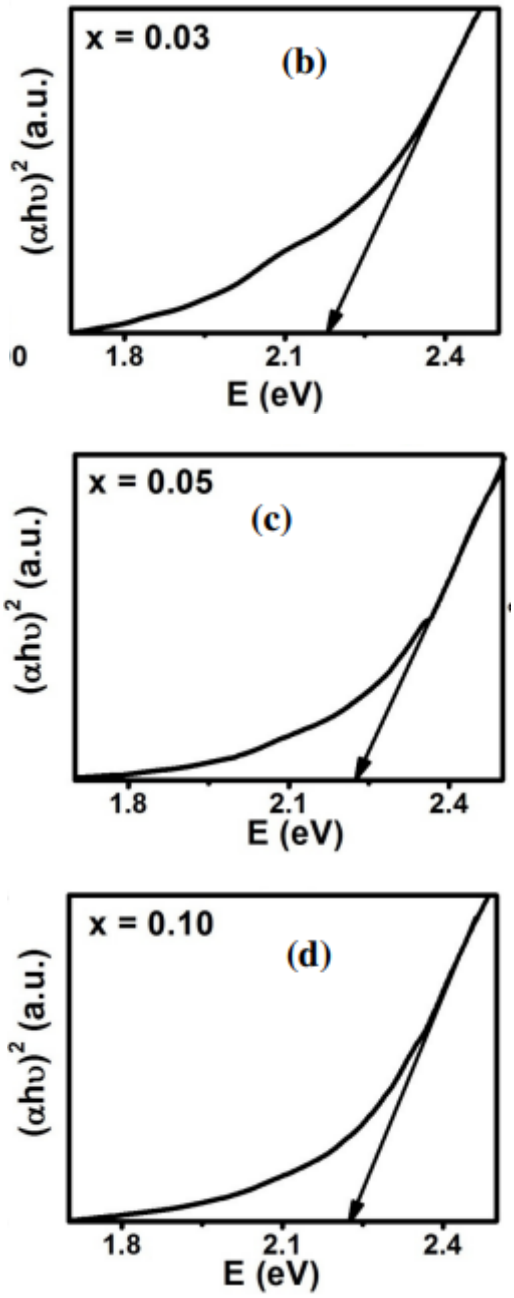

FTIR Studies

We can use infrared spectroscopy to identify the materials that will be used to build bonds. For example, the Fourier transform infrared (FTIR) spectrum has peak frequencies which correlate to the vibrations of the atoms present in the sample. This indicates a fingerprint of a sample. None 2item have the same infrared spectrum due to the fact that each has a distinct atom arrangement. Bond formation among different elements may be determined via FTIR analysis. KBr pellets were used to record the FTIR spectra of all samples. Figure 14 depicts the FTIR spectra of $Bi_{1-x}Dy_xFeO_3$samples at room temperature in the 400-1000 cm-1 wave number range. The vibration zones of 550 cm-1 and 443 cm-1 are plainly discernible. These bands are assigned to the stretching and bending oscillations of Fe-O in the FeO6 octahedral unit. As well as having absorption ranges at 530 cm-1 as well as 450 cm-1, the octahedral structural unit of BiO_6 displays a number of other properties.

Figure 14

FTIR transmittance spectra for $Bi_{1-x}Dy_xFeO_3$nanoparticles

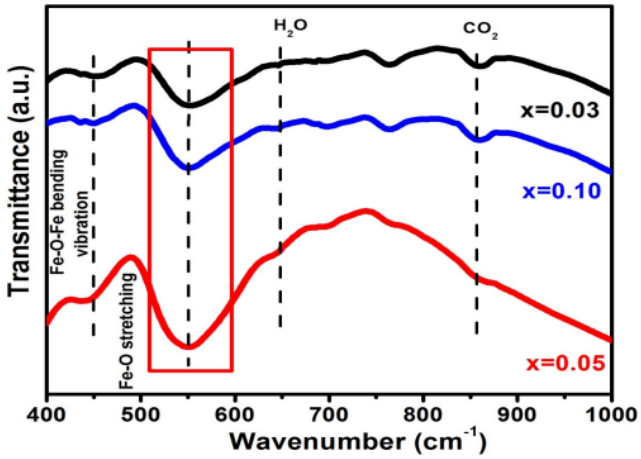

The retention maxima of FeO6octahedra& BiO6octahedra occur at about the comparable wave number, bringing about the presence of expansive vibration groups. The third top at 573 cm-1 shows an out-of-ease vibration of oxygen's premise molecules in the rhombohedral BFO. The creation of a metal-oxygen link confirms the establishment of the perovskite structure. Grain boundaries in nano-sized crystals are distinct from the bulk crystal's atoms or molecules, As a consequence, overall length as well as coordination are disrupted. The shifting of FTIR spectra is caused by this loss of symmetry.

Gaussian pinnacle fitting was utilized in the wave no. band of 500 cm-1 to 620 cm-1 to work out the metal oxide bond length and the impact of Dy doping on the bond length (a-c). The plots show that when Dy3+ particles supplant Bi3+ particles, The 533.14 cm-1 stage advances to 528.16 cm-1, while the 548.16 cm-1 mode leaps to 552.60 cm-1.

Figure 15

Adjusted FTIR absorption spectra in the 500-620 cm-1 band of wavelengthfor $Bi_{1-x}Dy_xFeO_3$ nanoparticles.

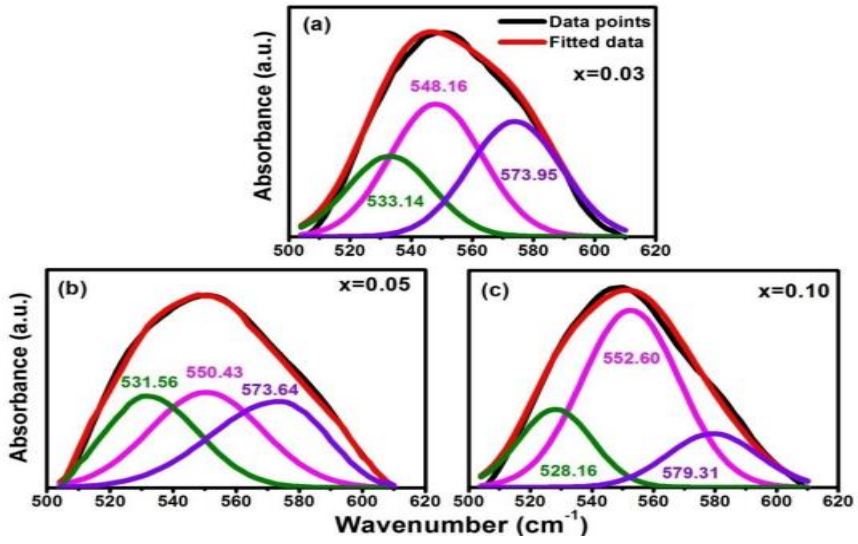

Bi/Dy-O and Fe-O bonds' vibrational frequencies may be found using the following relation:

$$\nu = \frac{1}{2\pi c}\sqrt{(K/\mu)}$$

There are two types of bonds: Bi/Dy-O and Fe-O, both of which have an average force constant of K. As μ added bonus, the bond's effective mass may be calculated through the relation:

$$\mu = \frac{M_o \times \left[xM_{Bi} + (1-x)M_{Dy}\right]}{M_o + \left[xM_{Bi} + (1-x)M_{Dy}\right]} \quad (7)$$

As well as

$$\mu = \frac{M_o \times M_{Fe}}{M_o + M_{Fe}} \quad (8)$$

Where,M_o,M_{Bi}, $M_{Dy}$and$M_{Fe}$are the O's atomic masses, Bi, Dy, as well as Fe correspondingly.Force constant (K) could be associated to the mean$Bi/(Dy) - O$ and $Fe - O$ bond lengths (r) by the formula

$$K = 17/r^3 \quad (9)$$

Table 4 shows the results of utilizing the formulae to determine the accurate mass, force constant, as well as bond angle. As shown in the figure, the change in bond length in each sample is consistent with the XRD pattern Rietveld refinement findings.

Table 4 The FTIR spectra of $Bi_{1-x}Dy_xFeO_3$nanoparticles were used to compute the Wave no, effective mass, force constant, and bond lengths are all factors to consider.

Parameters		0.03	0.05	0.10
Wave no. (cm-1)	(Fe-O)	550.05	551.22	5523.59
	(Bi-O)	535.14	530.99	530.16
μ (10-26Kg)	(Fe-O)	2.079	2.079	2.079
	(Bi-O)	2.490	2.490	2.485
K (Ncm-1)	(Fe-O)	2.511	2.493	2.460
	(Bi-O)	2.220	2.240	2.260
(Å)	(Fe-O)	1.969	1.970	1.959
(FTIR)	(Bi-O)	1.995	1.900	1.905
(Å)	(Fe-O)	2.156	2.072	2.030
(Rietveld)	(Bi-O)	2.405	2.470	2.539

Conclusions

Utilizing the tartaric corrosive methodology, we have effectively created Bi1-

xDyxFeO3nanoparticles with x upsides of 0.03, 0.05, and 0.10. The effect of Dy substitution on the microstructure and mechanical properties of BiFeO3 were explored. The rhombohedral to orthorhombic stage change for the x=0.10 test was affirmed by XRD and Raman measurements.One of the main properties of frail magneticity is that it requires an octahedral pivot of the oxygen particles. The expanded attraction in the examples was connected with contortions in turn cycloid design and ferromagnetic communication among Dy3+ particles and Fe3+ particles. The consideration of Dy3+ particles has been displayed to expand the dielectric attributes of the materials examined. As far as photocatalytic movement and optoelectronic gadgets, for x = 0.03 to 0.10 examples, the band hole of nanoparticles ranges from 2.12 to 2.22 eV. The FTIR spectra showed different speculatively expected tops related to the formation of Bi-O and Fe-O bonds, and the determined bond lengths still up in the air by Rietveld examination.

References

1. W. Eerenstein, N.D. Mathur, J.F. Scott, Multiferroic and magnetoelectric materials, Nature 442 (2006) 759.
2. R. Ramesh, N.A. Spaldin, Multiferroics: progress and prospects in thin films, Nature Materials 6 (2007) 21.
3. J. Wang, J.B. Neaton, H. Zheng, V. Nagarajan, S.B. Ogale, B. Liu, et al., Epitaxial BiFeO3 Multiferroic Thin Film Heterostructures, Science 299 (2003) 1719.
4. C. Ederer, N.A. Spaldin, Weak ferromagnetism and magnetoelectric coupling in bismuth ferrite, Physical Review B: Condensed Matter 71 (2005) 060401.
5. J. Liu, M. Li, L. Pei, J. Wang, Z. Hu, X. Wang, X. Zhao, Effect of Ce and Zr codoping on the multiferroic properties of BiFeO3 thin films EPL 89 (2010) 57004.
6. M. Kumar, K.L. Yadav, G.D. Verma, Large magnetization and weak polarization in sol–gel derived BiFeO3 ceramics, Materials Letters 62 (2008) 1159.
7. B. Yu, M. Li, Z. Hu, L. Pei, D. Guo, X. Zhao, S. Dong, Enhanced multiferroic properties of the high-valence Pr doped BiFeO3 thin film, Applied Physics Letters 93 (2008) 182909.
8. V.A. Khomchenko, V.V. Shvartsman, P. Borisov, W. Kleemann, D.A. Kiselev, I.K. Bdikin, J.M. Vieira, A.L. Kholkin, Effect of Gd substitution on the crystal structure and multiferroic properties of BiFeO3, Acta Materialia 57 (2009) 5137.
9. N.V. Minh, N.G. Quan, Structural, optical and electromagnetic properties of Bi1−xHoxFeO3 Multiferroic, Journal of Alloys and Compounds 509 (2011) 2663.
10. S. Zhang, W. Luo, D. Wang, Y. Ma, Phase evolution and magnetic property of Bi1−xDyxFeO3 ceramics, Materials Letters 63 (2009) 1820.
11. M. Kumar, K.L. Yadav, Study of room temperature magnetoelectric coupling in Ti substituted bismuth ferrite system Journal of Applied Physics 100 (2006) 074111.
12. S. Chauhan, M. Kumar, S. Chhokar, S.C. Katyal, H. Singh, M. Jewariya, K.L. Yadav, Multiferroic, magnetoelectric and optical properties of Mn doped BiFeO3 nanoparticles Solid State Communications 152 (2012) 525.
13. P. Uniyal, K.L. Yadav, Observation of the room temperature magnetoelectric effect in Dy doped BiFeO3, Journal of Physics: Condensed Matter 21 (2009) 012205.

14. Xu J.M., Wang G.M., Wang H.X., Ding D.F., He Y., Synthesis and weak ferromagnetism of Dy-doped BiFeO3 powders", Mater. Lett. vol. 63, pp.855, 2009.
15. Zhang S.T., Zhang Y., Lu M.H., Du C.L., Chen Y.F., Liu Z.G., Zhu Y.Y. , Ming N.B.,Pan X.Q., "Substitution-induced phase transition and enhanced multiferroic properties of Bi1-xLaxFeO3 ceramics", Appl. Phys. Lett., vol. 88, pp. 162901, 2006.
16. Yuan G.L., Or S.W., "Multiferroicity in polarized single-phase Bi0.875 Sm0.125FeO3 ceramics", J. Appl. Phys., vol. 100, pp. 024109, 2006.
17. Liu J., Fang L., Zheng F.G., Ju S., Shen M.R., "Enhancement of magnetization in Eu doped BiFeO3 nanoparticles", Appl. Phys. Lett., vol. 95, pp. 022511, 2009.
18. Muneeswaran M., Jegatheesan P., Gopiraman M., Kim I-S., Giridharan N.V., "Structural, optical, and multiferroic properties of single phased BiFeO3", Appl. Phys. A, DOI 10.1007/s00339-013-7712-5.
19. Singh M.K., Ryu S., Jang H.M., "Polarized Raman scattering of multiferroic BiFeO3 thin films with pseudo-tetragonal symmetry", Phys. Rev. B, vol. 72, pp. 132101, 2005.
20. Yang Y., Sun J.Y., Zhu K., Liu Y.L., and Wan L., "Structure properties of BiFeO3 films studied by micro-Raman Scattering", J. Appl. Phys., vol. 103 pp. 093532, 2008.
21. Ramirez M.O., Krishnamurthi M., Denev S., Kumar A., Yang S.Y., Chu Y.H., Saiz E., Seidel J., Pyatakov A.P., Bush A., Viehland D., Orenstein J., Ramesh R., Gopalan V., "Two-phonon coupling to the antiferromagnetic phase transition in multiferroic BiFeO3", Appl. Phys. Lett., vol. 92, pp. 022511, 2008.
22. Pandit P., Satapathy S., Gupta P.K., "Effect of La substitution on conductivity and dielectric properties of Bi1-xLaxFeO3 ceramics: An impedance spectroscopy analysis", Phys. B, vol. 406, pp. 2669, 2011.
23. Watcharapasorn A., Jiansirisomboon S., "Grain growth kinetics in Dy-doped Bi0.5 Na0.5TiO3 ceramics", Ceram. Int., vol. 34, pp. 769, 2008.
24. Qian F.Z., Jiang J.S., Guo S.Z., Jiang D.M., Zhang W.G., "Multiferroic properties of Bi1−xDyxFeO3 nanoparticles", J. Appl. Phys., vol. 106, pp. 084312, 2009.
25. Jeon N., Rout D., Kim W., Kang S.J.L, "Enhanced multiferroic properties of single-phase BiFeO3 bulk ceramics by Ho doping", Appl. Phys. Lett., vol. 98 pp. 072901, 2011.
26. Qian F.Z., Jiang J.S., Jiang D.M., Zhang W.G., Liu J.H., "Multiferroic properties of Bi0.8Dy0.2−xLaxFeO3 nanoparticles", J. Phys. D: Appl. Phys., vol. 43, pp. 025403, 2010.
27. Zhu W.M., Su L.W., Ye Z.G., Ren W., "Enhanced magnetization and polarization in chemically modified multiferroic (1-x)BiFeO3–xDyFeO3 solid solution", Appl. Phys. Letts., vol. 94, pp. 142908, 2009.
28. Jonscher A.K., "The `universal' dielectric response", Nature, vol. 267, pp. 673, 1977.
29. Srivastava A., Singh H.K., Awana V.P.S., Srivastava O.N., "Enhancement in magnetic and dielectric properties of La and Pr co substituted BiFeO3", J. Alloys Compd., vol. 552, pp. 336, 2013.
30. Makhdoom A.R., Akhtar M.J., Rafiq M.A., Hassan M.M., "Investigation of transport behavior in Ba doped BiFeO3", Ceramics International, vol. 38, pp. 3829, 2012.
31. Kumar A., Yadav K.L., Rani J., "Low temperature step magnetization and magnetodielectric study in Bi0.95La0.05Fe1−xZrxO3 ceramics", Materials Chemistry

and Physics, vol. 134, pp. 430, 2012.
32. Uniyal P., Yadav K.L., "Pr doped bismuth ferrite ceramics with enhanced multiferroic properties", J. Phys.: Condens. Matter. vol. 21, pp. 405901, 2009.
33. Singh H., Yadav K.L., "Effect of Nb substitution on the structural, dielectric and magnetic properties of multiferroic BiFe1−xNbxO3 ceramics", Materials Chemistry and Physics, vol. 132, pp. 17, 2012.
34. Mishra R.K., Pradhan D.K., Choudhary R.N.P., Banerjee A., "Effect of yttrium on improvement of dielectric properties and magnetic switching behavior in BiFeO3", J. Phys.: Condens. Matter. vol. 20, pp. 045218, 2008.
35. Catalan G., Scott J.F., “Physics and applications of bismuth ferrite”, Advanced Materials, vol. 21, pp. 2463, 2009.
36. Reetu, Agarwal A., Sanghi S., Ashima, "Rietveld analysis, dielectric and magnetic properties of Sr and Ti codoped BiFeO3 multiferroic", J. Appl. Phys., vol. 110, pp. 073909, 2011.
37. Pandit P., Satapathy S., Gupta P.K., “Effect of La substitution on conductivity and dielectric properties of Bi1-xLaxFeO3 ceramics: An impedance spectroscopy analysis”, Phys. B, vol. 406, pp. 2669, 2011.
38. Chang D.A., Lin P., Tseng T.Y., "Optical properties of zrtio4 films grown by radiofrequency magnetron sputtering", J. Appl. Phys., vol. 77, pp. 4445, 1995.
39. Liu Z., Qi Y., Lu C., "High efficient ultraviolet photocatalytic activity of BiFeO3 nanoparticles synthesized by a chemical coprecipitation process", J. Mater. Sci.: Mater. Electron. vol. 21, pp. 380, 2010.
40. Guo R., Fang L., Dong W., Zheng F., Shen M., "Enhanced Photocatalytic Activity and Ferromagnetism in Gd Doped BiFeO3 Nanoparticles", J. Phys. Chem. C, vol. 114, pp. 21390, 2010.
41. Mukherjee A., Hossain S.K., Pal M., Basu S., "Effect of Y-doping on optical properties of multiferroics BiFeO3 nanoparticles", Appl. Nanosci., vol. 2, pp. 305, 2012.
42. Joshi U.A., Jang J.S., Borse P.H., Lee J.S., "Microwave synthesis of singlecrystalline perovskite BiFeO3 nanocubes for photoelectrode and photocatalytic applications", Appl. Phys. Lett., vol. 92, pp. 242106, 2008.
43. Bhushan B., Basumallick A., Bandopadhyay S.K., Vasanthacharya N.Y., Das D., "Effect of alkaline earth metal doping on thermal, optical, magnetic and dielectric properties of BiFeO3 nanoparticles", J. Phys D: Appl. Phys. vol. 42, pp. 065004, 2009.